Chemical Engineering Journal 489 (2024) 151241

Contents lists available at ScienceDirect

Chemical Engineering Journal

journal homepage: www.elsevier.com/locate/cej

Designing a NiFe-LDH/MnO_2 heterojunction to improve the photocatalytic activity for NOx removal under visible light

María Ángeles Oliva [a], David Giraldo [b,c], Paloma Almodóvar [c], Francisco Martín [d], María Luisa López [b], Ivana Pavlovic [a], Luis Sánchez [a,*]

[a] Departamento de Química Inorgánica, Instituto de Química para la Energía y Medioambiente. Universidad de Córdoba, Campus de Rabanales, E-14014 Córdoba, Spain
[b] Departamento de Química Inorgánica, Facultad de Ciencias Químicas, Universidad Complutense de Madrid, Avda. Complutense s/n, 28040 Madrid, Spain
[c] Albufera Energy Storage, Hermosilla, 48-1° Dcha, 28001 Madrid, Spain
[d] Departamento de Ingeniería Química, Facultad de Ciencias, Universidad de Málaga, Campus de Teatinos, E-29071 Málaga, Spain

ARTICLE INFO

Keywords:
LDH
Birnessite
Heterojunction
Photocatalysis
Nitrogen Oxides
Depollution

ABSTRACT

2D/2D heterojunctions between ultrathin NiFe-CO_3 layered double hydroxide (LDH) and varying amounts of birnessite (δ-MnO_2) were prepared using an environmentally friendly and cost-effective self-assembly method. The prepared samples have proven to be efficient in their application, mitigating NOx emissions via a photo-oxidative process. The effective creation of 2D/2D NiFe–LDH/MnO_2 heterojunctions has been verified through a variety of characterisation techniques, such as XRD, FT-IR, TGA, XFR, N_2 adsorption–desorption isotherms, HRTEM and SEM images, EDX, and XPS. Photocatalytic measurements have indicated that the heterojunction formed between NiFe-LDH and MnO_2 modifies its photoconductive behaviour, significantly enhancing the visible light photocatalytic performance of the partners. Finally, the optimal relationship between NiFe-LDH and MnO_2 in the photocatalytic process was studied. It was found that a ratio of 10:1, respectively, exhibited superior properties compared to the other composites, highlighting the best performance in the degradation of NO under visible light and notable stability during the recycling process.

1. Introduction

The rapid development of industry and population growth has caused a deterioration of air quality worldwide, particularly impacting urban areas. Nitrogen oxides (NOx = NO + NO_2) are among the pollutants in atmospheric chemistry that have raised significant global concern due to their toxicity and persistence, posing serious threats to human health and the environment [1,2]. Therefore, there is an urgent need for the design of remediation strategies to eliminate these pollutants from the atmosphere, while adhering to established annual limits [3]. This necessity has driven the development of NOx emission mitigation technologies, collectively referred to as DeNOx action, with the most common methods being selective catalytic reduction (SCR), non-selective catalytic reduction (NSCR), NOx storage catalyst. Other options include NOx absorption, phase separation, ozone injection or NO to HNO_3 conversion. Since the early 21st century, photocatalysis has been considered an ideal air purification method due to its environmental compatibility, low energy consumption, mild conditions and the utilisation of sunlight, atmospheric water, and oxygen molecules as reactants. In fact, numerous research studies have widely demonstrated the effectiveness of photocatalysts for DeNOx action [4–7]. However, the use of advanced photocatalysts still faces some challenges such as poor harvesting of the entire solar spectrum, toxicity, low DeNOx selectivity and poor profitability [8–11]. Most of the photocatalysts known to date are active under UV light ($\lambda < 400$ nm), but their response under visible light is often limited. It is essential to meet this requirement in order to ensure their effectiveness, especially for application in urban environments where external radiant energy will not be employed, and where UV light exposure can vary due to meteorological or geographical conditions. Therefore, developing new photocatalysts capable of functioning not only under UV light, but also exhibiting a strong performance under visible light, is of utmost importance. In the pursuit of new photocatalysts which respond to visible-spectrum light, electronic heterojunctions stand out as a compelling strategy by creating new pathways that allow the mobility of charge carriers (e^-/h^+) and delay their prompt recombination [12–17].

Additionally, transition metals enhance the appeal of this approach, given their low-cost and low-toxicity characteristics. In this context,

* Corresponding author.
E-mail address: luis-sanchez@uco.es (L. Sánchez).

https://doi.org/10.1016/j.cej.2024.151241
Received 22 January 2024; Received in revised form 20 March 2024; Accepted 10 April 2024
Available online 12 April 2024

Layered Double Hydroxides (LDHs) represent a family of semiconductors that has recently been investigated and utilised for DeNOx applications [17–22]. Thanks to the inherent properties of its structure, LDH has demonstrated excellent performances and outstanding selectivity toward the oxidation of NO into nitrite/nitrate species [23–27]. The flexibility of the composition allows the modification of the band gap and band position over a broad range [20,28], enhancing the light absorbance capacity, facilitating the separation of charge carriers, and promoting the generation of appropriate reactive oxygen species (ROS). Furthermore, the layered structure enables the attainment of ultrathin dimensions (2D) by reducing the thickness along the c-axis, thereby increasing the specific surface area and providing more active centers available for reactants [29]. The 2D-LDHs have been previously reported to boost the DeNOx performance, thus serving as a promising platform for constructing new heterojunctions. On the other hand, as a transition metal oxide, MnO_2 has attracted attention in the photocatalytic field given its ability to boost visible light response due to its narrow band gap (~1.9 eV) [30–32]. Some of the most notable properties of this p–type semiconductor are the high thermal stability and the multiple inherent oxidation states (+2, +3, +4, +6 and + 7), that benefit exposing charge carriers. Up to the present, some composites based on LDH/MnO_2 have been previously reported [33–35] but, as far as we know, no other studies have utilized them as a photocatalyst for air remediation. Herein, we present a type-I heterojunction formed by the union of NiFe-LDH and δ-MnO_2 nano-layered compounds. NiFe-LDH/MnO_2 composites were obtained by a simple and environmentally friendly method, using abundant and low-cost raw materials. An exhaustive study of their physicochemical and optical properties has revealed valuable advantages over their precursors resulting in a multicomponent photocatalyst with superior characteristics. These include greater accessibility to the active sites, enhanced light absorption and improved separation of charge carriers (e^-/h^+), contributing to higher photocatalytic efficiency under visible light irradiation. The optimized composite demonstrates a remarkable efficiency in removing NO under visible light when compared to advanced photocatalysts addressing concerns related to cost, hazardous materials, environmental impact, and reusability.

2. Materials and methods

2.1. Materials

$NiCl_2{\cdot}6H_2O$ (Sigma Aldrich, 98 %), $FeCl_3{\cdot}6H_2O$ (PanReac AppliChem, 97 %), $Na_2CO_3{\cdot}10H_2O$ (PanReac AppliChem, 99 %), $KMnO_4$ (Sigma Aldrich, 99 %), NaOH (PanReac AppliChem, 98 %) ethanol (PanReac AppliChem, 99.5 %), and methanol (PanReac AppliChem, 99,9 %) chemicals were used to prepare the photocatalysts. For experiments related to the capture of reactive radical species: 5,5-Dimethyl-1-pyrroline N-oxide (DMPO, Sigma-Aldrich, 98 %), tert-butanol (t-BOH, Sigma-Aldrich, 99 %), p-benzoquinone (p-BQ, Sigma-Aldrich, 98 %), potassium dichromate ($K_2Cr_2O_7$, Sigma-Aldrich, 99.5 %), and potassium iodide (KI, DC PanReac, 99 %) were employed. All the reagents purchased were of a high degree of purity.

2.2. Synthesis of photocatalysts

2.2.1. Preparation of NiFe-LDH and MnO_2

$Ni_3Fe\text{-}CO_3$ LDH (labelled as NiFe-LDH) was synthesized via the co-precipitation method and subsequently delaminated following the AMOST (Aqueous Miscible Organic Solvent Treatment) procedure [36]. To obtain a Ni^{2+}/Fe^{3+} molar ratio equal to 3:1, a 1.0 M metal solution was prepared by dissolving 0.75 M $NiCl_2{\cdot}6H_2O$ and 0.25 M $FeCl_3{\cdot}6H_2O$ into 100 mL of deionised water. Successively, the metal solution was dropped into 0.125 M of $Na_2CO_3{\cdot}10\ H_2O$ solution while stirring for 1 h. In order to set the pH at 10 ± 0.2, a 4 M NaOH solution was automatically added with an auto-titrator (Dosimat 725 and pH-meter 691 model, Metrohm). Following the previously published procedure [37], the resulting suspension was stirred for 16 h at room temperature and then filtered and washed with deionised water until pH = 7 was obtained. Subsequently, the wet cake was washed, dispersed for 6 h in pure ethanol and filtered. Finally, the wet solid was dried in a stove at 60 °C overnight. Approximately 8 g powder of NiFe-LDH was obtained.

Birnessite (δ-MnO_2) was synthesised through the thermal decomposition of 1.0 g (6.32 mmol) of $KMnO_4$ powder, subjected to a temperature of 400 °C for 5 h, and exposed to air. The process involved a heating and cooling rate of 10 °C per minute. The final product was thoroughly washed with deionised water until pH = 7 was reached, and dried in a stove at 80 °C overnight [38]. The sample was labelled as MnO_2.

2.2.2. Preparation of NiFe/MnO_2 composites

NiFe/MnO_2 composites were prepared by a simple self-assembly procedure outlined in Scheme 1 in Supplementary Information (SI). Initially, different amounts of the prepared MnO_2 powder (10, 30 and 60 mg) were dispersed in 5 mL of an ethanol solution. Simultaneously, in a different vessel, 100 mg of the NiFe–LDH was dispersed in 20 mL of ethanol. Both solutions underwent ultrasound treatment to segregate particles. After dispersion (1 h), the solutions were combined in a beaker at room temperature for 18 h under continuous stirring. They were then subjected to centrifugation and dried overnight at 60 °C. The synthesized samples were named NiFe/MnO_2-0.1, NiFe/MnO_2-0.3 and NiFe/MnO_2-0.6, respectively.

2.3. Characterisation techniques

The chemical composition, morphology, structure and optical properties of the samples were studied using the following techniques:

- X-ray powder diffraction (XRD) patterns were registered on a Bruker D8 Discover X-ray diffractometer at room temperature using monochromatic Cu–Kα radiation with λ = 1.5406 Å. Data were recorded in the $5° < 2\theta < 70°$ range with a step size of 0.04° and 1.05 s per step.
- Fourier transform infrared (FT-IR) spectra were recorded employing a PerkinElmer Spectrum Two spectrophotometer in the 450–4000 cm^{-1} region with a diamond accessory of Attenuated Total Reflection (ATR) mode.
- The chemical composition of the samples was measured by X-ray fluorescence (XRF) employing a Rigaku ZSX Primus IV spectrometer equipped with a 4 kW rhodium anode and a scintillation counter for heavy elements.
- High-resolution transmission electron microscopy (HRTEM) analysis was conducted using a JEOL 300FEG. The preparation of the samples involved crushing the powders in n-butanol and dispersing them onto copper grids coated with a porous carbon film.
- Scanning electron microscopy (SEM) images were obtained with a JSM 7600F microscope and a Bruker AXS 4010 detector for energy dispersive X-ray spectroscopy (EDX). The samples were pre-dried at 50 °C for 48 h and affixed to SEM stubs using carbon adhesive before being sputter-coated with graphite.
- Thermogravimetric analyses (TGA) were performed on a Mettler Toledo TGA/DSC 1 Star System in the temperature range 30–600 °C with 50 mL min^{-1} of an O_2 flow and a temperature elevation rate of 5 °C min^{-1}. To carry out the experiments, 70 μl Al_2O_3 crucibles containing approximately 10 mg of sample were used.
- N_2 adsorption–desorption isotherms were analysed in a Micromeritics ASAP 2020 instrument. Before analysis, the samples underwent overnight vacuum degassing at 90 °C. Subsequently, measurements were conducted at 77.4 K with liquid nitrogen as the adsorbent. Calculations of specific surface areas and pore size distributions were performed employing the Brunauer–Emmett-Teller (BET) within the relative equilibrium pressure interval $0.05 < P/P_0 < 0.30$.

- Ultraviolet–visible diffuse reflectance (UV–vis DRS) measurements were developed in a Cary 5000 UV–Vis-NIR spectrophotometer equipped with an integrating sphere with a photomultiplier/PbS detector. Teflon was employed as the reference for equipment calibrations and scans were registered from 200 to 800 nm.
- X-ray photoelectron spectroscopy (XPS) analysis was performed using a Physical Electronics PHI 5700 spectrometer equipped with a multichannel hemispherical detector and a non-monochromatic Mg Kα radiation (300 W, 15 kV, 1253.6 eV std). The refined scan spectra were acquired with a step energy of 29.35 eV and an analysis area of 720 μm. The spectrometer's energy scale calibration utilized the Cu $2p_{3/2}$, Ag $3d_{5/2}$ and Au $4f_{7/2}$ photoelectron lines with binding energies (B.E.) 932.7, 368.3 and 84.0 eV, respectively. The samples were positioned in a sample holder with metal wells and sustained in a high-vacuum state within the preparation chamber, prior to their transfer to the analysis chamber. Maintaining a residual pressure below 8.0 x 10–9 Torr, the spectrum acquisition process was carried out in the analysis chamber. Software MultiPak version 9.3 (Copyright Ulva-phi, Inc) was employed to fit the XPS peaks with Gaussian/Lorentzian bands (Shirley Background subtraction, and Chi-Square as fit test).

2.4. Evaluation of the photocatalytic activity

The photocatalytic performance was assessed by a DeNOx test, in which the photocatalyst inside a reaction chamber was exposed to light illumination while passing a continuous flow rate of NO gas. The experiment was performed by depositing 250 mg of powdered sample on a quartz sample holder (50 mm x 50 mm) and then placed in a laminar flow reactor chamber located inside a dark box equipped with an ultraviolet Xe lamp (Solarbox 3000e RH model; light irradiance: 25 and 500 W m^{-2} for UV and Vis light, respectively) and a visible LED lamp (Kessil PR160-427 nm model; $\lambda = 427$ nm; light irradiance: 510 W m^{-2}). A continuous stream comprising NO gas and humid air was connected to the reactor chamber. In order to replicate urban atmospheric conditions, the concentration levels were set to 150 ppb with a flow gas = 0.325 l min^{-1} and relative humidity (RH) equal to 40 ± 5 % by splitting zero air through a gas-washing bottle containing demineralised water. The outlet gases were circulated to a chemiluminescent analyzer (Environement AC 32 M) which measures the concentration of NO, NO_2 and NOx gases in situ. The equations of the DeNOx (E_{NO}, E_{NO2}, E_{NOx}) and Selectivity (S) performance indexes are defined in SI.

The photocatalytic mechanism was elucidated from data obtained through electron paramagnetic resonance (EPR), diffuse reflectance infrared Fourier transform spectroscopy (DRIFTS) and scavengers measurements. EPR spectra were acquired at room temperature on an EMXmicro spectrometer (Bruker) and operating with an X band frequency of approximately 9.83 GHz. DRIFTS assessments were registered at room temperature with a Perkin Elmer Frontier FT-IR spectrometer equipped with a Harrick Praying Mantis diffusion reflection accessory and reaction chamber.

Additional information concerning the photocatalytic activity evaluation is provided in SI.

3. Results and discussion

3.1. Samples characterisation

X-ray diffraction (XRD) patterns of MnO_2, NiFe-LDH and the corresponding NiFe/MnO_2 composites are shown in Fig. 1A. The MnO_2 sample crystallised into birnessite phase, as evidenced by its X-ray diffractogram displaying prominent reflections at 2θ values of approximately ~12.4° (7.1 Å) and ~24.9° (3.6 Å), corresponding to the characteristic (00 l) and (002 l) reflections, characteristic of these structures. Additionally, at 2θ values around ~36.5° (2.5 Å) and ~65.5° (1.4 Å), two *hk* bands are identified with the (20,11) and (02,31)

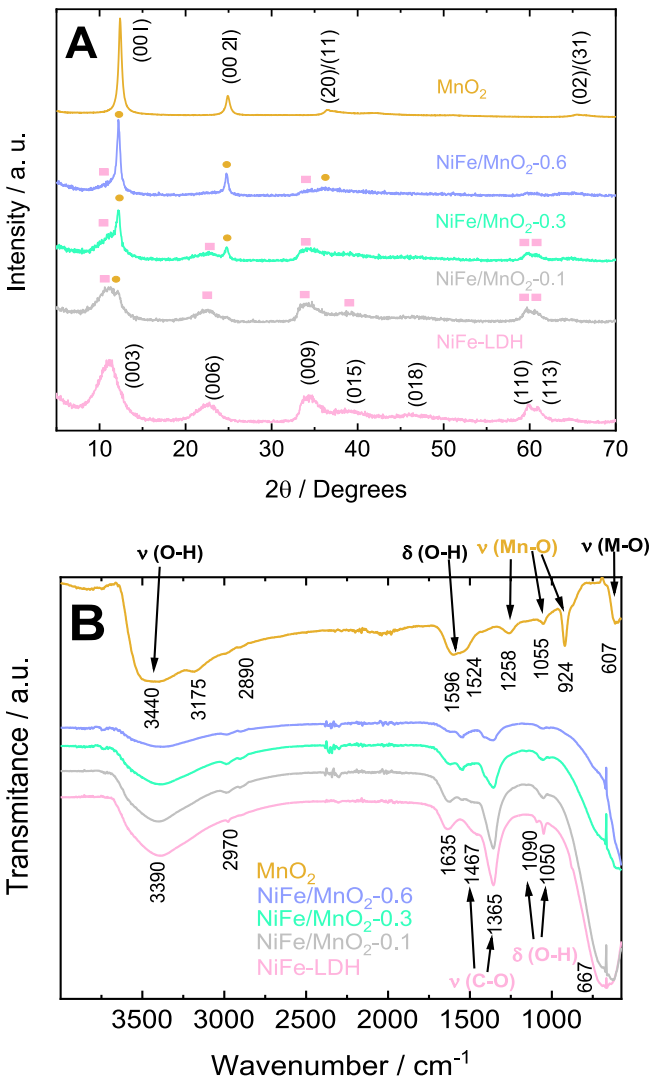

Fig. 1. (A) XRD patterns and (B) FT-IR spectra for the MnO_2, NiFe-LDH and NiFe/MnO_2 samples.

reflections [39]. These observations suggest the existence of a diffusive pattern associated with turbostratic disorder in the examined sample. Additionally, it is worth noting that the characterization of the MnO_2 sample has already been reported by some of us [38], which includes the XRD structural refinement of the K_xMnO_2 compound locating K^+ and H_2O species in the interlayer space. In the case of the layered double hydroxide, the NiFe-LDH sample exhibits broad and low-intensity basal XRD reflections associated with its 2D character. Layered double hydroxides (LDHs) constitute a vast family of compounds whose structure derives from that of brucite ($Mg(OH)_2$), with partial isomorphous substitution of divalent ions by trivalent ones. A positive charge thus created within the hydroxide layers is balanced by the intercalation of hydrated anions in the interlayer space. Their general formula can be written as $[MII_{1-x}MIII_x(OH)_2]^{x+}A_n^{-x/n}\cdot mH_2O$, where MII is the divalent ion (Mg^{2+}, Zn^{2+}, Ni^{2+}, etc.), MIII the trivalent ion (Al^{3+}, Fe^{3+}, Cr^{3+}, etc.) and X^{n-} is the interlayer anion (Cl^-, CO_3^{2-}, SO_4^{2-}, etc.) [40]. In order to obtain a nano-layered LDH, as commented in the experimental section, this sample is prepared using the AMOST procedure which promotes the LDH delamination decreasing the layer stacking [29]. The typical reflections indicative of an LDH structure were observed, with planes located at 2θ–11.2° (7.96 Å), 22.7° (3.94 Å) and 34.27° corresponding to the basal (003), (006) and (009) planes, and others situated at angles higher than 2θ, corresponding to (015), (018), (110) and (113) planes

[29]. For the composites, the XRD patterns reveal the main reflections of both raw materials, suggesting the formation of a well-defined heterostructure. The observed reflections in the NiFe/MnO_2 samples were mainly the basal planes of both structures, (0 0 3), (0 0 6) and (0 0 9) for NiFe, and (00 l) and (002 l) for MnO_2. Notably, these basal planes exhibited the same 2θ angle for both partners, indicating the absence of an intercalation process between the layered compounds. Due to the disparity in crystallinity between the two compounds, distinguishing reflections attributed to the layered double hydroxide phase becomes challenging as the concentration of MnO_2 increases in the composite. Additional information about the structure/composition of the samples was obtained from the FT-IR spectra, Fig. 1B. The NiFe-LDH spectrum displays bands indicative of O-H stretching vibrations (3390 cm^{-1}) and the H-O-H bending vibration of the interlayer water molecules (1635 cm^{-1}). The presence of carbonate located within the LDH interlayer is inferred by bands positioned at 1467 and 1365 cm^{-1}, while the appearance of bands at 2970, 1090 and 1050 cm^{-1} is attributed to the presence of trace amounts of ethanol molecules. The presence of these organic molecules remaining in the LDH structure is a result of their utilisation in the AMOST delamination process. Using this procedure, solvent molecules partially enter the interlayer galleries, displacing the H_2O molecules. As a result, the decrease in hydrogen bonding between layers promotes the delamination of LDH [37]. Finally, at lower frequencies (below 900 cm^{-1}), sharp bands are associated with the HO-M-OH and M-O and vibrational bending modes. In the FT-IR spectrum of the MnO_2 sample, as mentioned earlier, in the 4000–2000 cm^{-1} region, the H-O-H bending and O-H stretching vibrations of H_2O molecules are observed. Moreover, the band around 3175 cm^{-1} could be related to a certain form of the ordering of H_2O molecules in the structure [41]. The bands at around 1596 and 1524 cm^{-1} are associated with the bending of OH/H_2O. The band appearing at 924 cm^{-1} is linked to vibrations of peripheral Mn-O moving in conjunction with OH groups located on the edges of the particles [41]. In the composites, the most prominent feature is the predominance of bands characteristic of the LDH structure, primarily those associated to the carbonate vibrations modes. The variation in the intensity of these bands indicates the different quantities of NiFe-LDH present in the composites. The most notable observation is the absence of bands associated with Mn-O vibrations adjacent to OH groups in all prepared composite samples, including the disappearance of the shoulder at 3175 cm^{-1} and the band at 924 cm^{-1}. Therefore, the absence of bands associated with Mn-OH interactions in all prepared composites suggests a significant modification in the surface structure, likely associated with the anchoring of MnO_2 nano-particles onto NiFe-LDH nanolayers. This structural alteration should indicate an enhanced interaction between both materials and a modification of the photoconductive behaviour.

The chemical formula of the raw materials was determined from results obtained using XRF and TGA techniques, Figs. S1 and S2 and Table S1a. In the case of NiFe-LDH, as before mentioned, the amount of carbonate anions was presumed to be essential for balancing the positive charge of the metal hydroxide layers. The M^{2+}/M^{3+} ratio was 2.92, near the theoretical one of 3.0. In the MnO_2 material, a K/Mn ratio of 0.3 was determined. The elemental composition was confirmed by EDX analysis, Table S1b. Given that the content of K is equal to the content of Mn(III), it is acceptable to deduce a Mn(III)/Mn(IV) ratio which provides insights into the potential correlation between the photocatalytic activity of these composites and the presence of Mn(III) in the material. The oxidation states for the elements in both compounds were deduced from XPS results, as further discussed in section 3.3.

3.2. Morphology, textural and optical properties

The MnO_2, NiFe-LDH and NiFe/MnO_2 samples appear as aggregates of nanoparticles, as shown in Fig. S3. The corresponding EDX mapping images of the elements Ni, Fe, Mn, and K reveal their complete dispersion in both the raw samples and the composites, indicating a notable homogeneous distribution in the heterostructure (Figs. S4–S7). HRTEM images reveal the 2D nature of the nanoparticles observed for the studied compounds, Fig. 2. The HRTEM images of MnO_2 particles reveal a distance between layers close to ~7 Å corresponding to (00 l) planes of the lamellar structure, Fig. 2B. NiFe-LDH consists of flower-like particles formed by corrugated nanosheets with a thickness ranging from 3–5 nm, as illustrated in Fig. 2C. In Fig. 2D, the high-resolution TEM image of NiFe-LDH shows a lattice spacing of ~8 Å, associated to d_{003} of LDH, (Fig. 1A). The 2D morphology of MnO_2 and NiFe–LDH nanoparticles is preserved in the prepared composites, Fig. 2E. The HRTEM images show the attached MnO_2 nanoparticles onto NiFe-LDH nano-layers validating the effective interaction between both systems within the NiFe/MnO_2 composites (Fig. 2F and S8). Distances of ~7 Å can be associated with the interlayer distances (00 *l*) of the MnO_2 phase due to the turbostratic effect and exhibiting higher transmission contrast, related to its greater thickness.

Because of the significance of available active sites for the catalytic heterogeneous reactions, an analysis of the specific surface area of the samples was conducted using N_2 adsorption–desorption isotherms, as depicted in Fig. 3A. The isotherm shapes exhibited characteristics consistent with a type II isotherm. Notably, the NiFe-LDH sample

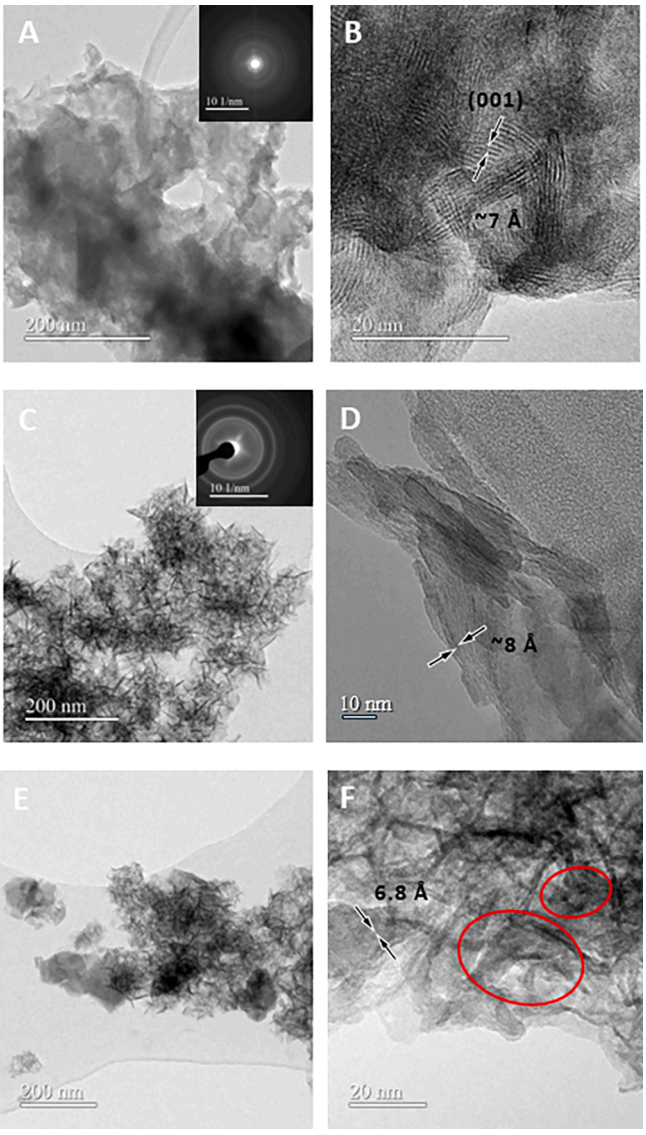

Fig. 2. HRTEM images of the (A-B) MnO_2, (C-D) NiFe-LDH and (E-F) NiFe/MnO_2-0.1 samples.

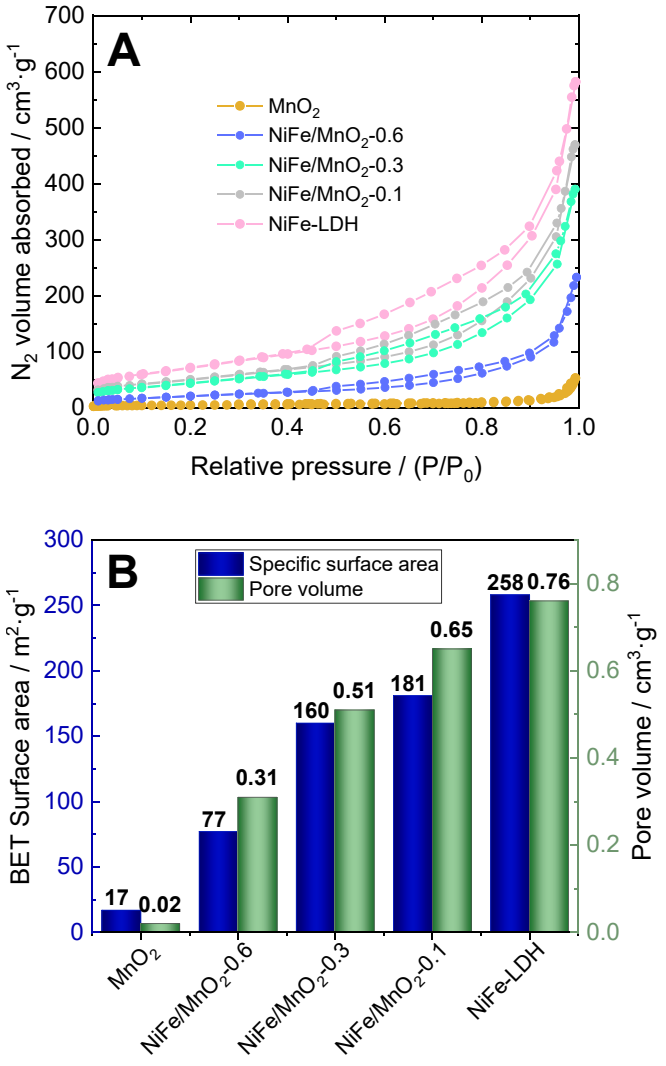

Fig. 3. (A) N_2 adsorption–desorption isotherms and (B) BET surface area and pore volume for the MnO_2, NiFe-LDH and NiFe/MnO_2 samples.

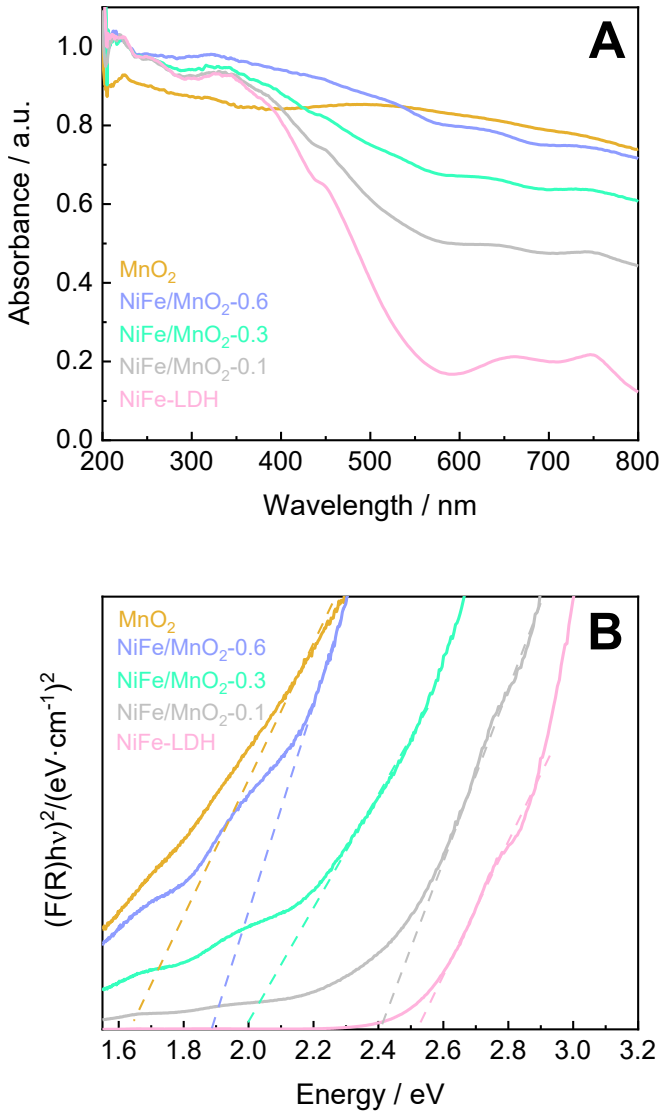

Fig. 4. (A) UV–Vis absorption spectra and (B) Kubelka-Munk transformed function plot for the MnO_2, NiFe-LDH and NiFe/MnO_2 samples.

displayed an H3 hysteresis loop, a distinctive feature associated with LDHs obtained by the AMOST procedure [37]. In concordance with the observations from HRTEM images, this structure is attributed to the presence of slit-shaped pores, a consequence of the sheet-shaped morphology. In the case of the composites, the hysteresis loop became shorter as the amount of NiFe-LDH decreased. In contrast to MnO_2, NiFe-LDH exhibits a significantly higher specific surface area (258.4 vs. 16.6 $m^2\ g^{-1}$) and pore volume (0.76 vs. 0.02 $cm^3\ g^{-1}$), as illustrated in Fig. 3B. This notable increase is attributed to the successful delamination of numerous nano-sheets accounted within the LDH structure when the AMOST procedure is applied [29]. The specific surface area of the composites increases with the NiFe-LDH content, providing a larger number of active sites. Consequently, an enhanced photocatalytic performance is expected.

The study of the optical characteristics was determined with the diffuse reflectance UV–Vis absorption technique, as shown in Fig. 4A. NiFe-LDH exhibits a pronounced absorbance in the UV spectrum (200–400 nm) but also significant bands in the visible region. The bands attributed to UV light absorption are linked with ligand-to-metal electron transitions within an octahedral environment. Conversely, the broad bands in the 600–800 nm range can be associated with *d-d* transitions of the metals composing the layers [29]. In the case of MnO_2, a strong absorption in the ultraviolet and visible region is observed, similar to that previously reported in the literature [42,43]. The band gap values (E_g) for each sample were calculated from the transformed Kubelka-Munk function, Fig. 4B. The estimated energy gap of NiFe-LDH, NiFe/MnO_2–0.1, NiFe/MnO_2-0.3, NiFe/MnO_2-0.6 and MnO_2 are 2.5 eV, 2.3 eV, 2.0 eV, 1.9 eV and 1.6 eV, respectively. In contrast to NiFe-LDH, the visible light harvesting of composites is enhanced by the presence of MnO_2, which should help generate electron-hole pairs crucial for photochemical reactions.

3.3. Photocatalytic DeNOx performance and mechanism

The photocatalytic activity of the samples was evaluated based on their capacity to abate nitrogen oxide gas from the air, thus serving as an environmental tool to clean polluted atmospheres. To perform the DeNOx experiments, the samples were placed in a continuous flow photoreactor, and light irradiated. Fig. S9A depicts the measured values of NO concentration as a function of time. During the equilibrium process in the absence of light ($0 < t < 10$ min) the NO measured is that of the inlet NO concentration (150 ppb), indicating that no reaction occurs in the chamber. Subsequently, once the UV–Vis lamp is on ($t = 10$ min), a rapid decline in NO concentration is noted, arriving at a steady state 20 min after light exposure ($t = 30$ min). Finally, in the dark, the NO concentration is recovered when the lamp is off ($t > 70$ min). The

concentration profile observed is associated with the occurrence of a photocatalytic reaction. Upon light irradiation with the appropriate photon energy, charge separation occurs. The excited electrons move to the conduction band (CB), creating holes in the valence band (VB). Before their recombination, both charges can react with molecules absorbed on the surface of the photocatalysts, primarily oxygen and water vapour molecules present in the air. Consequently, highly reactive oxygen species (ROS species) such as hydroxyl (·OH) and superoxide (O_2^-) radicals are formed. These radicals then react with the environmental molecules in contact with the photocatalyst, the NOx gases in our case. Following this photochemical oxidation process, the NOx gases are effectively removed from the air as they transform into nitrate and nitrite species [6], as discussed below. For the first time, the use of MnO_2 as a DeNOx photocatalyst is here reported. Despite its very small specific surface area (16.6 $m^2\ g^{-1}$), the MnO_2 photocatalyst exhibits a very interesting ability to remove NOx gases under UV–Vis light irradiation, with an E_{NO} efficiency of 63 %, as shown in Fig. S9B. This observed high activity is in line with those reported for δ-MnO_2 photocatalysts, for which a high surface Mn^{4+}/Mn^{3+} molar ratio favours a better photochemical activity [44]. This E_{NO} value clearly surpasses those reported for transition metal oxides studied as DeNOx photocatalysts, Table S2, making it intriguing and warrants further investigation in future studies. On the other hand, NiFe-LDH exhibits an outstanding DeNOx efficiency with a value of $E_{NO} = 77$ % in line with those reported for AMOST LDHs, for which their large surface area exposed to the gas reactant molecules help to boost their ability to remove them from air [21,29].

During the photochemical process, NO_2 gas is produced as an intermediate product of the oxidation of NO to NO_3^-. It is important to avoid the release of NO_2 into the atmosphere, as it is significantly more toxic than NO [45], thereby achieving a high selectivity in the formation of the nitrate phase. Once formed, the large surface area of NiFe-LDH facilitates the adsorption of NO_2 molecules onto the photocatalyst surface [29] and, therefore, their oxidation to nitrates, avoiding their release to the atmosphere. In this sense, the NiFe-LDH photocatalyst is highly selective towards the DeNOx process, S = 94 %. In the case of MnO_2, the selectivity is limited to S = 78 %. Overall, both photocatalysts exhibit significant ability to remove NOx gases, with E_{NOx} values of 50 % and 72 % for MnO_2 and NiFe-LDH, respectively (Fig. S9B). However, this ability is seriously limited when the photocatalyst works under visible light illumination, Fig. 5A. Thus, the activity of the MnO_2 photocatalyst proves to be negligible with $E_{NO} = 6$ % and that of NiFe-LDH decays to a poor value of $E_{NO} = 22$ %. A similar low efficiency for the NO abatement under visible light was previously reported for the NiFe-LDH system [22].

As mentioned in the introduction section, the development of photocatalysts capable of working under visible light is crucial for environmental applications. In this context, the preparation of NiFe/MnO_2 heterostructures proves to be fundamental in enhancing the visible light activity of these photocatalytic systems, leading to a noticeable increase in the E_{NO} values (Fig. 5A and 5B). The ratio of NiFe/MnO_2 is important in optimising the photocatalytic performance. The activity seems to be mainly governed by the NiFe-LDH partner and the increasing amount of MnO_2 in the heterostructure resulted in a poorer DeNOx performance. This activity can be attributed to the fact that the latter masks numerous active sites on the NiFe photocatalyst surface and diminishes the specific surface area of the composite (Fig. 3B). It is important to highlight that a near full DeNOx selectivity, S ≈ 98 %, was preserved for NiFe/MnO_2 photocatalysts (Fig. 5B). The NiFe/MnO_2-0.1 sample emerges as the optimal heterostructure with an $E_{NO} = 41$ % (Fig. 5B), a good value in line with the majority of previously reported visible light DeNOx photocatalysts, Table S3. Furthermore, focusing on its potential application as a visible light photocatalyst for the DeNOx process, the NiFe/MnO_2-0.1 sample underwent several consecutive photocatalytic tests to assess the long-term efficacy and stability (Fig. S10). The sample exhibits a low tendency to decrease the E_{NO} efficiency, reaching a value of 34 % after the fourth run. This is attributed to the production of NO_3^- and NO_2^-

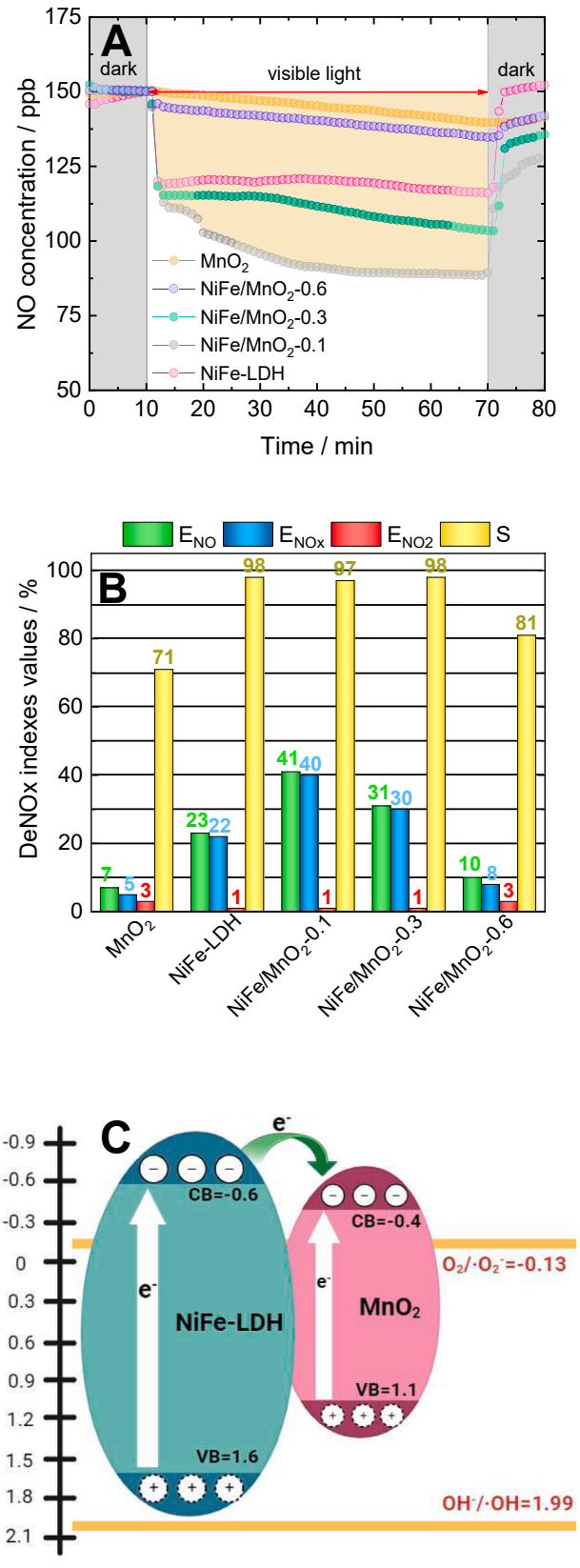

Fig. 5. (A) Nitrogen oxide concentration profiles and (B) DeNOx indexes during the photocatalytic test under visible light (λ = 427 nm) obtained for the MnO_2, NiFe-LDH and NiFe/MnO_2 samples. (C) Schematic energy band diagrams for the NiFe-LDH and MnO_2 samples.

species during the photochemical conversion of NO, as will be discussed later. These species progressively accumulate on the surface, masking some of the active sites of the photocatalyst and thereby detrimentally affecting its performance. However, the high solubility of nitrite/nitrate species allows for their easy elimination from the photocatalyst's surface through a simple washing procedure with Milli-Q water. Therefore, after washing, collecting, and drying the photocatalyst following the fourth run the E_{NO} index returns to similar values (5^{th} run) as those observed for the pristine sample (1^{st} run). In addition, the stability of the photocatalyst was assessed through XRD HRTEM and XPS characterization and no structural, morphological, and chemical changes were observed after the photocatalytic process (Figs. S11 and S12). This highlights the high DeNOx efficiency and resilience of these photocatalysts. The obtained results, compared with those reported for photocatalysts in Table S3, show the promising advantages for the future implementation of NiFe/MnO_2-0.1 as a DeNOx photocatalyst. Most photocatalysts are highly selective, and some of them exhibit a higher E_{NO} efficiency, however, these are based on expensive (e.g., Pd, Eu, QDs) or toxic (e.g., Pd, Pb) elements. In contrast, the reusability of NiFe/MnO_2-0.1 was maintained for more than double the duration (6 h of experiment) compared to the majority of photocatalysts studied (1–2.5 h). For practical applications, the future use of DeNOx photocatalyst to combat polluted urban atmospheres requires large quantities of material with good photocatalytic efficiency, a simple preparation methodology, the use of low-cost and non-toxic elements, and enhanced reusability. Considering Table S3, all requirements are met by the NiFe/MnO_2-0.1 sample.

To explain this enhanced photocatalytic behaviour, Fig. 5C shows a schematic diagram of the theoretical band structure for the NiFe/MnO_2 interface. The positioning of the valence band (VB) and conduction band for each partner was proposed based on the previous literature for δ-MnO_2 and Ni_3Fe-LDH photocatalysts [46,47]. The energy level diagram could be described as a type-I heterojunction that was successfully used in previous photocatalytic processes in air and water [48,49]. While the indicated energy positions may not precisely correspond to the edges of the absolute conduction band (CB) and valence band (VB) of both semiconductors, these values serve as a reference to delve into the electronic interaction between the individual constituents of the heterostructure. Under light exposure, the photogenerated electrons reach the CB in NiFe-LDH. Since the CB in NiFe-LDH lies at more negative potential values, a flow of electrons towards CB in MnO_2 is expected. This proposed charge transfer mechanism should suppress the detrimental charge carrier recombination in the highly active NiFe-LDH photocatalyst, thereby positively influencing the ultimate DeNOx visible light ability of the material.

Different experiments were conducted to corroborate the theoretical mechanism proposed. Firstly, the XPS characterisation of MnO_2, NiFe-LDH, and NiFe/MnO_2-0.3 samples was carried out, by recording the C 1s, O 1s, Ni 2p, Mn 2p, Mn 3 s, and Fe 2p XPS regions. C 1s at 284.8 eV was used for charge shift correction, Fig. S13A. The O 1s peak for NiFe-LDH appears at 531 eV (Fig. S13B) while the O 1s peak for MnO_2 can be deconvolved into three peaks at 530 eV, 531.5 eV and 533.1 eV, corresponding to Mn-O-Mn, M−O−H, and H-O-H, respectively (Fig. S13B and Fig. S13C). Fig. 6A shows the characteristic pattern of the Ni $2p_{3/2}$ (855.6 eV) and Ni $2p_{1/2}$ (873.3 eV) and the two satellites Ni $2p_{3/2}$ and Ni $2p_{1/2}$. The binding energy of 855.6 eV for Ni $2p_{3/2}$ indicates a Ni^{2+} hydroxide chemical environment, conforming to previously reported results [29,50]. Fig. 6B shows the XPS Fe 2p region. The pattern, along with shake-up satellite peaks, centred around the binding energy of Fe $2p_{3/2}$ at 711.5 eV corresponds to Fe^{3+} hydroxide [50]. Both results confirm the proposed formula of $[Ni_{0.74}Fe_{0.26}(OH)_2](CO_3)_{0.13}$ for the NiFe-LDH sample. Fig. 6C shows the Mn 2p region for the MnO_2 sample, and Fig. 6D the Mn 3 s. Mn 3 s shows two multiplet split components caused by the coupling of non-ionized 3 s electrons with 3d valence band electrons. The binding energy separation between this multiple split has been reported to be around 5.8 eV, 5.5 eV, 5.4 eV and 4.7 eV for MnO,

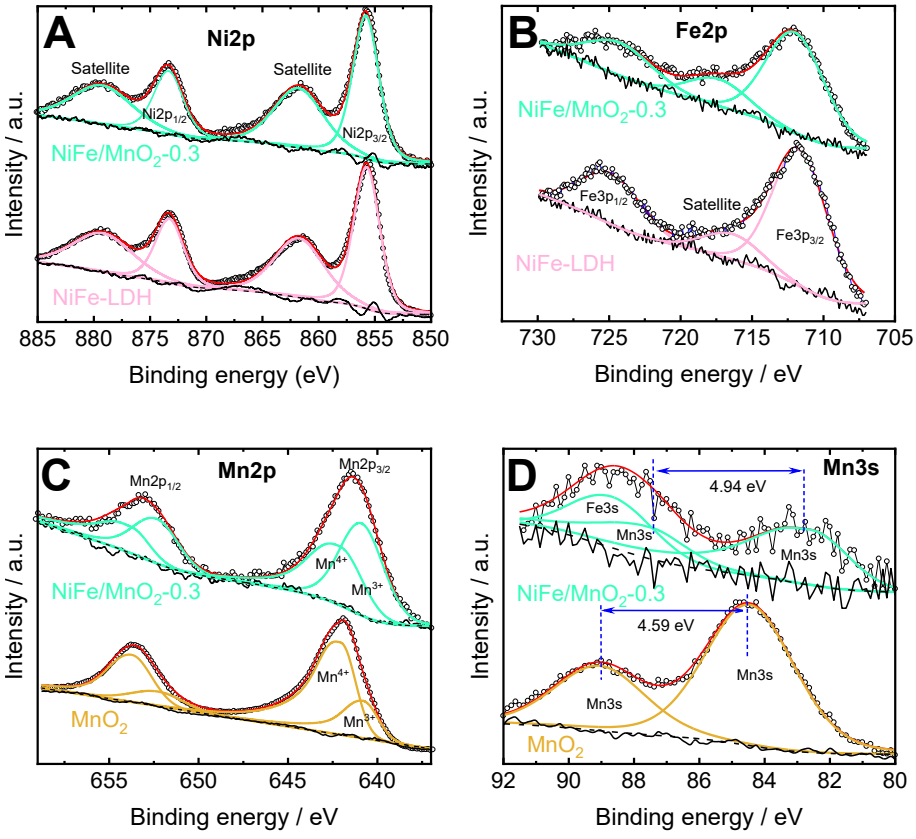

Fig. 6. XPS spectra, (a) Ni 2p, (b) Fe 2p, (c) Mn 2p and (d) Mn 3 s regions, obtained from the surface of the MnO2, NiFe-LDH and NiFe/MnO_2-0.3 samples.

Mn_3O_4, Mn_2O_3 and MnO_2, respectively [51,52]. The separation between the two multiplet split components of Mn 3 s was $\Delta E_{Mn3s} = 4.59$ eV (Fig. 6D) for MnO_2. Finally, by applying the equation of Beyreuther et al. ($\nu_{Mn} = 9.67 - 1.27\ \Delta E_{Mn3s}$) [53] an average oxidation state of $\nu_{Mn} = 3.8$ was estimated. This value is related to the presence of Mn^{3+}, in correspondence with the chemical formula $K_{0.3}MnO_2{\cdot}0.3H_2O$ (Table S1), and provides the area ratio for deconvolution of the Mn 2p XPS region (around 20 % Mn^{3+}, 80 % Mn^{4+}), Fig. 6C. The peaks at 641.3 eV and 642.4 eV (Mn $2p_{3/2}$) are assigned to Mn^{3+} and Mn^{4+}, respectively [50]. The asymmetry of the peaks is associated with a combination of Mn oxidation states. The measured K 2p signal confirms the presence of K^+ ions in the MnO_2 sample, Fig. S14. Noticeable changes were observed in XPS signals for the NiFe/MnO_2-0.3 sample. Thus, the Fe 2p peaks undergo a shift towards a more oxidated state, as shown in Fig. 6B, whereas the Mn 2p signal suffers a shift at lower binding energies corresponding to an increase in Mn^{3+}, Fig. 6C. The Mn $2p_{3/2}$ Mn^{3+}/Mn^{4+} area ratio for NiFe/MnO_2-0.3 (Fig. 6C) provides an estimate of the Mn average oxidation state of 3.4 (60 % Mn^{3+}, 40 % Mn^{4+}). Using the Beyreuther et al. equation, the binding energy separation of the Mn 3 s multiplet is $\Delta E_{Mn3s} = 4.94$ eV. The positions of the peaks of Mn 3 s are more influenced by the formal charge of the manganese ion than in the case of Mn 2p, and suffer a shift to higher energies with an increase in the oxidation state [54]. The deconvolution Mn 3 s region of NiFe/MnO_2-0.3 (Fig. 6D) is affected by the overlapping of the Fe 3 s signal, and a weaker signal of the Mn 3 s and Fe 3 s. There is no change in the oxidation state of the Ni (Fig. 6A). The XPS findings agree with the theoretical band structure proposed for the NiFe/MnO_2 interface (Fig. 5C), the CB electrons of NiFe-LDH partner being drained by the MnO_2 and confirming the creation of a good electronic heterojunction.

The EPR measurements helped identify the reactive species participating in the photochemical process. Fig. 7 shows the EPR signals obtained for the photocatalysts DMPO as the spin trapping agent in aqueous and methanolic solutions. In the case of aqueous solutions, the DMPO−•OH adduct signal is usually observed when holes originated during the photocatalytic process have enough redox potential to convert water molecules or hydroxyl groups into hydroxyl radical ($E_{\cdot OH/H2O} = 2.82$ eV; $E_{\cdot OH/OH^-} = 1.99$ eV). In this context, the formation of •OH radicals (Fig. 5C) is impeded as the valence band (band) edge in each material is positioned below 2.82 eV (or 1.99 eV) of energy. However, intense signals are observed for the MnO_2 photocatalyst and the composites with a higher amount of MnO_2. In fact, an intense heptaplet signal is observed for MnO_2 even in the absence of light, Fig. 7A. This is associated with the powerful oxidation character of manganese dioxide in water, leading to a chemical rather than a photochemical reaction with DMPO.

This signal is characteristic of the corresponding nitroxide, DMPOX, formed during the oxidation reaction of DMPO [55–57]. On the other hand, in methanolic solutions, the sextet corresponding to the DMPO−•O_2^- adduct is observed. Its intensity increases with light irradiation time, indicating that superoxide radicals arise from the

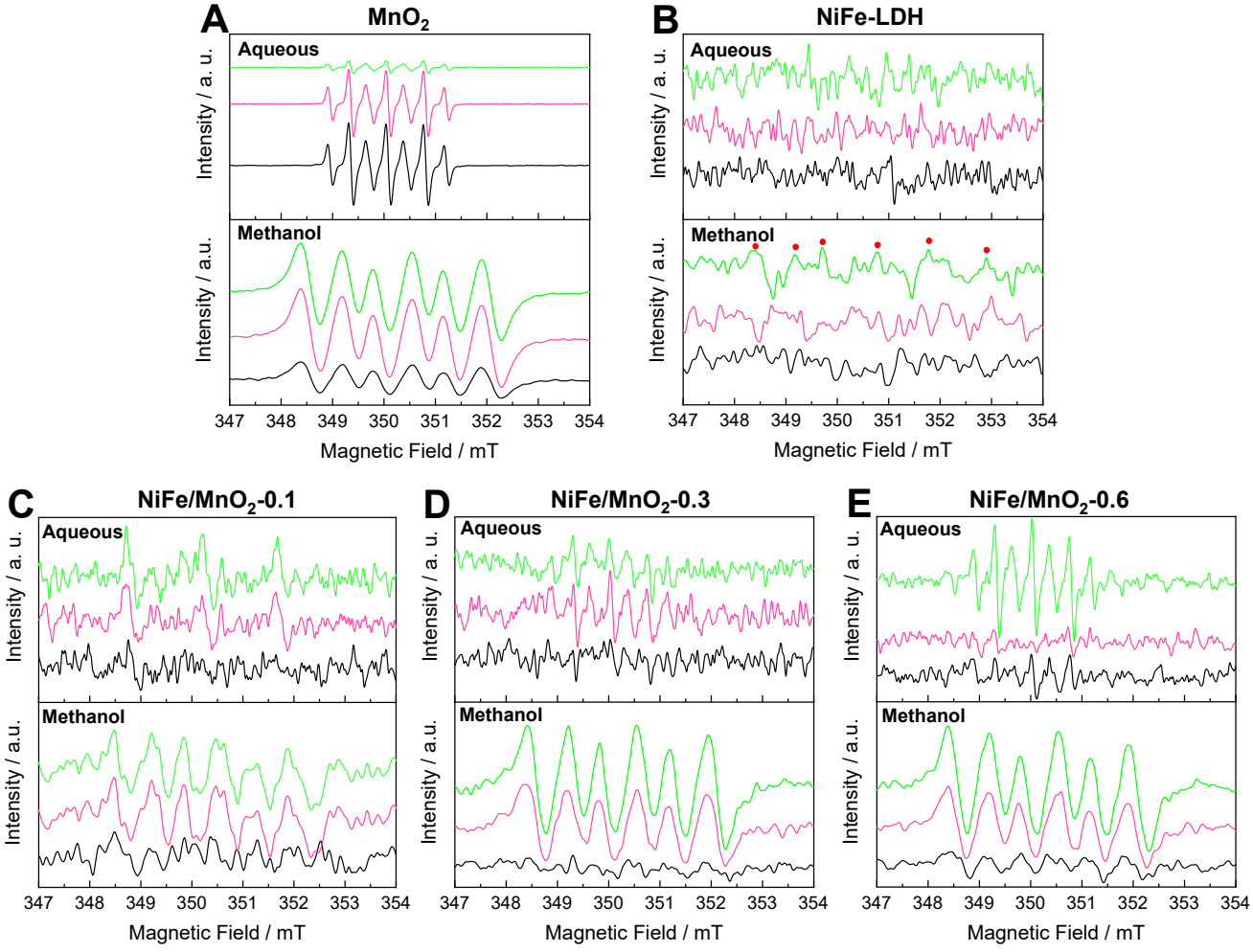

Fig. 7. DMPO spin-trapping EPR spectra of the (A) MnO_2, (B) NiFe-LDH and (C-E) NiFe/MnO_2 (0.1, 0.3 and 0.6, respectively) samples in aqueous solution and methanol solutions irradiated with a visible lamp of 427 nm of wavelength for 0, 5 and 10 min (black, pink and green, respectively).

photochemical process. This agrees with the theoretical positioning of the CB edge for the NiFe-LDH and MnO_2 photocatalysts (−0.6 and −0.4 eV, respectively), which is lower than the $O_2/\bullet O_2^-$ pair (− 0.13 eV).

In the case of MnO_2, the formation of superoxide radicals is expected to result from a chemical reaction, as previously reported [58], with their appearance beginning in dark conditions. The limited capability of NiFe-LDH to generate superoxide radicals under visible light has been previously reported [22]. Similarly, a negligible signal is measured after 10 min of light irradiation (Fig. 7B) explaining the observed low DeNOx activity (Fig. 5A). However, this ability is clearly reinforced by the formation of an electronic heterojunction with MnO_2 (Fig. 7C–E), which facilitates the flow of the electrons between CB from NiFe-LDH and MnO_2, as inferred from XPS data, and lessening the e^-/h^+ recombination in NiFe-LDH. It is interesting to highlight that, due to the intensity of the measured signals, higher amounts of superoxide radicals are produced for NiFe/MnO_2-0.3 and NiFe/MnO_2-0.6 photocatalysts; while NiFe/MnO_2-0.1, with better E_{NO} efficiency, showed a comparatively lower superoxide radical production (Fig. 5A and B). However, among the three composites, the NiFe/MnO_2-0.1 sample exhibits the largest specific surface area (Fig. 3B). This suggests that optimised photocatalytic activity results from a balance between electronic and physical properties in NiFe/MnO_2 composites. Thus, the NiFe/MnO_2-0.1 sample exhibits a lower ability to produce superoxide radicals but offers a higher number of active sites for NO reactant molecules. Therefore, the good DeNOx visible light activity of the formed heterostructure could be explained by facilitating the formation of radical species necessary to interact with the higher amount of gas molecules.

To confirm the role of charges and radicals in the photochemical mechanism under visible light, DeNOx experiments were conducted with the NiFe/MnO_2-0.1 sample using the corresponding scavengers (SI): tert-butanol (t-BOH), p-benzoquinone (p-BQ), KI and $K_2Cr_2O_7$ to trap hydroxyl radical species, superoxide radical species, holes, and electrons, respectively; Fig. 8. Once again, the pivotal role of superoxide radicals is confirmed, as the presence of p-BQ markedly hampers the elimination of NO. Similar behaviour is observed when electrons are trapped, both findings indicating the significance of both factors in the photochemical reaction. On the other hand, the NO concentration profile using t-BOH is similar to that exhibited by the photocatalyst in the absence of a scavenger, indicating that •OH radicals are not participating in the photochemical process, in accordance with EPR experiments. Interestingly, the h^+ charges also seem to play an important role in the DeNOx process, as the presence of KI abates the NO conversion. Because the positioning of the VB edges prevents the formation of •OH radicals, and they were not experimentally detected, the h^+ should be directly consumed in the oxidation of NO molecules to nitrite/nitrate species.

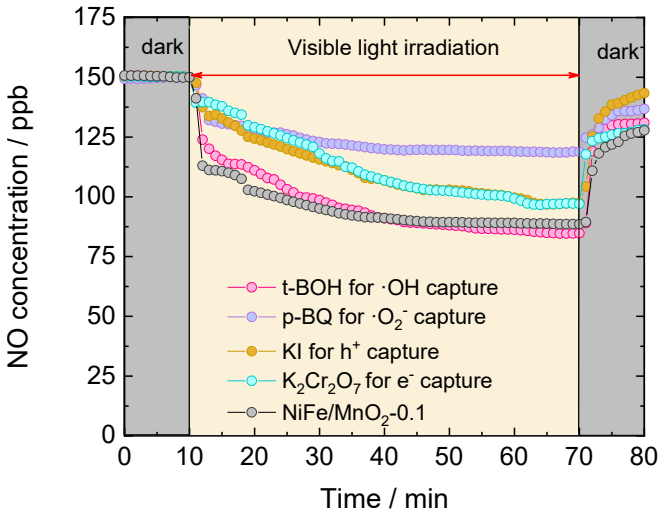

Fig. 8. Active species trapping experiments for the photocatalytic NO oxidation process over NiFe/MnO_2-0.1 sample.

Furthermore, DRIFTS assays were employed to gain insights into the interaction between NO molecules and the active surface of the photocatalyst, with the aim of elucidating the photochemical mechanism. The temporal evolution of the DeNOx process was measured in situ, as exhibited in Fig. 9. Preceding this, the samples underwent a pretreatment procedure, and a baseline spectrum was recorded. Sequential spectra were subsequently acquired as NO and O_2 were introduced into the reaction chamber, capturing variations under both dark and illuminated conditions. In the darkness, MnO_2 promotes a catalytic reaction of NO gas as indicated by low-intensity peaks associated with nitrite (1335, 1361 and 1460 cm^{-1}) and nitrate (1515, 1525 and 1570 cm^{-1}) species, as shown in Fig. 9A [15,29,59,60]. Upon illumination, there is an increase in the intensity of the signal and the appearance of new ones, indicating that a photochemical reaction is taking place. Thus, signals corresponding to bridged (bidentate) molecules of nitrate (1005, 1022, 1225, 1309 and 1548 cm^{-1}) as stabilised molecules on the surface of the photocatalyst are observed [61–63].

Additionally, the small bands located at 1394 and 1404 cm^{-1} are assigned to N_2O_4 as an intermediate appearing during the photochemical oxidation of NO [60]. In NiFe-LDH, a different profile is observed for the IR spectra obtained in the dark, Fig. 9B. The signal located at 1063 cm^{-1} corresponds to NO [61,64], indicating that gas molecules are easily adsorbed onto the photocatalyst surface, as previously observed for LDHs exhibiting a large specific surface area [29]. Subsequently, in the presence of the LDH's hydroxyl groups, the disproportionation of NO into NO^- (1127 cm^{-1}) and NO_2^- species (1288, 1330, 1367 and 1474 cm^{-1}) takes place. These species are ultimately oxidised to nitrate (1020, 1549 and 1566 cm^{-1}) in the presence of O_2. In the same way as MnO_2, once the NiFe-LDH is irradiated with light, intense signals for nitrite and nitrate species are measured due to the photochemical process taking place on its surface. Similar signals were identified during both the dark and illumination periods for the NiFe/MnO_2-0.1 sample (Fig. 9C). Interestingly, in the case of NiFe-LDH and NiFe/MnO_2-0.1 samples, the presence of NO bands (1063 cm^{-1}) is still observed under light irradiation. As previously reported [29], the large surface area of LDHs provides numerous unreacted active sites available on the surface to anchor NO gas molecules, thereby facilitating their subsequent photooxidation.

Finally, a plausible photochemical mechanism is proposed to explain the enhanced visible light DeNOx activity of NiFe/MnO_2 photocatalysts, as illustrated in Fig. S15. The proposed mechanism is supported by combined results obtained from XPS, EPR, DRIFTS and scavenger experiments. Under visible light irradiation, electrons in the VB are excited to reach the CB in both partners. Probably, in the MnO_2 semiconductor, the e^- and h^+ are immediately recombined, as the very high rate reported for this process on birnessite (10^{-11} s) [65], aligns with its negligible DeNOx activity (Fig. 5a). In the case of NiFe-LDH, the reported recombination rate is clearly slower ($1.57x10^{-9}$ s) [22], aligning with the superior DeNOx activity exhibited by this partner. In addition, thanks to the electronic heterojunction formed between the semiconductors, the e^-/h^+ recombination is reduced in NiFe/MnO_2 composites. This is achieved because electrons from CB in the NiFe-LDH are transferred to CB in MnO_2. As a result, both charge carriers (e^- in MnO_2 CB and h^+ in NiFe-LDH VB) can initiate the photo-oxidative DeNOx process, as summarised in Fig. S15. Thus, on the catalyst's surface, the formed superoxide radicals (2) promote the oxidation of NO to nitrate (3). This oxidation process may also involve the participation of holes reaching the catalyst's surface (4). Additionally, the holes could oxidate the lattice oxide ions to O^- (5), which are rapidly stabilised by the formation of nitrites (6). Ultimately, nitrites are converted to nitrates through the action of superoxides (7).

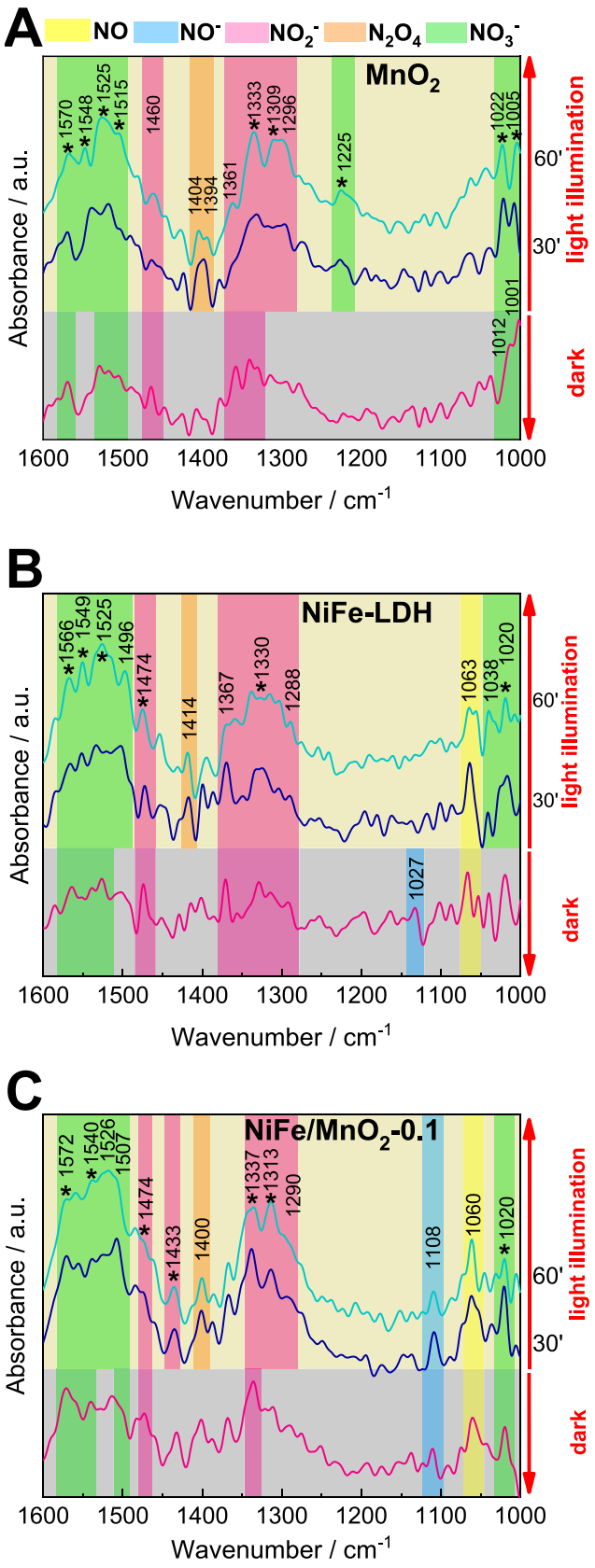

Fig. 9. In situ DRIFTs spectra for the (A) MnO_2, (B) NiFe-LDH and (C) NiFe/MnO_2-0.1 samples in dark conditions and under visible light irradiation (λ = 427 nm) recorded at 0, 30 and 60 min. Colour legend designated at the top of the figure for each of the different species generated during the process. (Asterisk denotes bidentate or chelate species).

4. Conclusions

2D/2D heterojunctions between NiFe-LDH and different amounts of MnO_2 (NiFe/MnO_2) were synthesised for application in the photocatalytic oxidation of NOx gases (DeNOx action). A simple self-assembly procedure, involving the mixing of ultrasonically dispersed ethanol suspensions of both NiFe-LDH and MnO_2, was implemented. A comprehensive characterisation study confirmed the successful attainment of the 2D/2D NiFe/MnO_2 composites. Although MnO_2 and NiFe-LDH photocatalysts show good efficacy in NOx gas removal under UV–Vis light irradiation, their DeNOx efficiency is significantly diminished under visible light, with E_{NO} = 6 % for MnO_2 and E_{NO} = 22 % for NiFe-LDH. DeNOx tests indicated that the formation of NiFe/MnO_2 heterojunctions significantly enhanced the visible light activity of these photocatalytic systems, resulting in a notable increase in E_{NO} values with exceptional selectivity for all samples (S = 98 %). The results showed that the sample with the highest NiFe–LDH amount, NiFe/MnO_2-0.1, has the best DeNOx efficiency (E_{NO} = 41 %) among NiFe/MnO_2 composites. A higher presence of NiFe-LDH in the sample provides a larger specific surface area, consequently offering more active sites on the surface to anchor NO gas molecules and facilitate their subsequent photo-oxidation. On the other hand, a lower but sufficient production of superoxide radicals is registered in this sample, suggesting that the optimised photocatalytic activity of NiFe/MnO_2 composites depends on both their electronic and physical properties. Results obtained from XPS, EPR, DRIFTS, and scavenger experiments suggest that the mechanism of the DeNOx process occurs via the photo oxidation of NO into nitrite/nitrate species and that the electronic heterojunction formed between the semiconductors reduces e^-/h^+ recombination. Additionally, the findings reveal the key role of superoxide radicals, indicating that •OH radicals do not participate in the photochemical process due to the position of the valence band edges in the heterojunction, preventing their formation. Finally, consecutive photocatalytic tests demonstrated the long-term efficacy and stability of the photocatalyst for DeNOx action. Compared to previously studied advanced DeNOx visible light photocatalysts, NiFe/MnO_2-0.1 composite emerges as a promising candidate for practical applications.

CRediT authorship contribution statement

María Ángeles Oliva: Writing – review & editing, Writing – original draft, Software, Methodology, Investigation, Data curation, Conceptualization. **David Giraldo:** Writing – review & editing, Writing – original draft, Methodology, Investigation, Data curation, Conceptualization. **Paloma Almodóvar:** Writing – review & editing, Validation. **Francisco Martín:** Writing – review & editing, Methodology, Investigation, Funding acquisition, Data curation. **María Luisa López:** Writing – review & editing, Writing – original draft, Validation, Supervision, Funding acquisition. **Ivana Pavlovic:** Writing – review & editing, Resources, Funding acquisition. **Luis Sánchez:** Writing – review & editing, Writing – original draft, Visualization, Validation, Supervision, Resources, Project administration, Methodology, Funding acquisition, Data curation, Conceptualization.

Declaration of competing interest

The authors declare that they have no known competing financial interests or personal relationships that could have appeared to influence the work reported in this paper.

Data availability

Data will be made available on request.

Acknowledgements

This work was financed by the Agencia Estatal de Investigación (Spain; MCIN PID2020-117516 GB-l00; PID2020-117516GB-l00/AEI/10.13039/501100011033), Albufera Energy Storage S.L. (151-2021) (A-2022) "Sistemas de almacenamiento energético". Mª Ángeles Oliva acknowledges a contract from the Spanish Government (FPU19/03570).

Appendix A. Supplementary data

Supplementary data to this article can be found online at https://doi.org/10.1016/j.cej.2024.151241.

References

[1] Air quality in Europe, report, Luxemburgo, Publications Office of the European Union, European Environment Agency, 2023 https://www.eea.europa.eu/publications/europes-air-quality-status-2023 (accessed 4 January 2024.
[2] World Health Organization, WHO global air quality guidelines (2021), Part. Matter (PM2.5 PM10), Ozone, Nitrogen Dioxide, Sulfur Dioxide Carbon Monoxide. https://iris.who.int/handle/10665/345329, (2021) 1–360 (accessed 4 January 2024).
[3] DIRECTIVE 2008/50/EC OF THE EUROPEAN PARLIAMENT AND OF THE COUNCIL of 21 May 2008 on ambient air quality and cleaner air for Europe. https://eur-lex.europa.eu/eli/dir/2008/50/oj, Chapter 15 Vol. 029. (2008) 169–212 (accessed 4 January 2024).
[4] J. Lasek, Y.H. Yu, J.C.S. Wu, Removal of NOx by photocatalytic processes, J. Photochem. Photobiol. C Photochem. Rev. 14 (2013) 29–52, https://doi.org/10.1016/j.jphotochemrev.2012.08.002.
[5] J. Ângelo, L. Andrade, L.M. Madeira, A. Mendes, An overview of photocatalysis phenomena applied to NOx abatement, J. Environ. Manage. 129 (2013) 522–539, https://doi.org/10.1016/j.jenvman.2013.08.006.
[6] L.S.M. Cruz-Yusta, M. Sánchez, Metal oxide nanomaterials for nitrogen oxides removal in urban environments, in: D.C. Maccato (Ed.), Wiley-VCH, From Design to Multi-Purpose Applications, Córdoba, Tailored Functional Oxide Nanomaterials, 2022, pp. 229–276.
[7] J.-C.-S.-W. Van-Huy Nguyen, Yu. Joseph Che-Chin, C.-W. Huang, Recent advances in the development of photocatalytic NOx abatement, Curr. Dev. Photocatal. Photocatalytic Mater. (2020) 211–229, https://doi.org/10.1016/B978-0-12-819000-5.00014-X.
[8] M. Nasirian, Y.P. Lin, C.F. Bustillo-Lecompte, M. Mehrvar, Enhancement of photocatalytic activity of titanium dioxide using non-metal doping methods under visible light: a review, Int. J. Environ. Sci. Technol. 15 (2018) 2009–2032, https://doi.org/10.1007/s13762-017-1618-2.
[9] Z. Li, S. Wang, J. Wu, W. Zhou, Recent progress in defective TiO2 photocatalysts for energy and environmental applications, Renew. Sustain. Energy Rev. 156 (2022) 111980, https://doi.org/10.1016/j.rser.2021.111980.
[10] Committee for Risk Assessment RAC, Opinion proposing harmonised classification and labelling at EU level of Titanium dioxide, EC Number: 236-675-5 CAS Number: 13463-67-7, Echa. http://echa.europa.eu/harmonised-classification-and-labelling-consultation/, 2017 (accessed 4 January 2024).
[11] V.H. Nguyen, B.S. Nguyen, C.W. Huang, T.T. Le, C.C. Nguyen, T.T. Nhi Le, D. Heo, Q.V. Ly, Q.T. Trinh, M. Shokouhimehr, C. Xia, S.S. Lam, D.V.N. Vo, S.Y. Kim, Q. Van Le, Photocatalytic NOx abatement: recent advances and emerging trends in the development of photocatalysts, J. Clean. Prod. 270 (2020) 121912, https://doi.org/10.1016/j.jclepro.2020.121912.
[12] J. Low, J. Yu, M. Jaroniec, S. Wageh, A.A. Al-Ghamdi, Heterojunction photocatalysts, Adv. Mater. 29 (2017), https://doi.org/10.1002/adma.201601694.
[13] K. Wang, C. Miao, Y. Liu, L. Cai, W. Jones, J. Fan, D. Li, J. Feng, Vacancy enriched ultrathin TiMgAl-layered double hydroxide/graphene oxides composites as highly efficient visible-light catalysts for CO2 reduction, Appl. Catal. B Environ. 270 (2020) 118878, https://doi.org/10.1016/j.apcatb.2020.118878.
[14] J. Fragoso, A. Pastor, M. Cruz-Yusta, F. Martin, G. de Miguel, I. Pavlovic, M. Sánchez, L. Sánchez, Graphene quantum dots/NiTi layered double hydroxide heterojunction as a highly efficient De-NOx photocatalyst with long persistent post-illumination action, Appl. Catal. B Environ. 322 (2023), https://doi.org/10.1016/j.apcatb.2022.122115.
[15] M.A. Oliva, J. Ortiz-bustos, M. Cruz-yusta, F. Martin, I. Hierro, 2D / 2D NiTi-LDH / BiOBr photocatalyst with extraordinary NO x removal under visible light, 470 (2023). https://doi.org/10.1016/j.cej.2023.144088.
[16] J. Zhang, X. Zan, X. Shen, H. Zheng, Preparation of direct Z-scheme hierarchical MoS2/MnO2 composite for efficient adsorption and wide spectrum photocatalytic degradation of organic pollutants in water, Mater. Res. Bull. 165 (2023) 112301, https://doi.org/10.1016/j.materresbull.2023.112301.
[17] H. Tang, X. Luo, W. Li, Y. Pan, S. Wang, H. Ma, Y. Shen, R. Fang, F. Dong, Highly active Ag/ZnO/ZnAl-LDH heterojunction photocatalysts for NO removal, Chem. Eng. J. 474 (2023) 145873, https://doi.org/10.1016/j.cej.2023.145873.
[18] H. Sun, Z. Chu, D. Hong, G. Zhang, Y. Xie, L. Li, K. Shi, Three-dimensional hierarchical flower-like Mg-Al-layered double hydroxides: fabrication, characterization and enhanced sensing properties to NOx at room temperature, J. Alloys Compd. 658 (2016) 561–568, https://doi.org/10.1016/j.jallcom.2015.10.237.
[19] F. Rodriguez-Rivas, A. Pastor, C. Barriga, M. Cruz-Yusta, L. Sánchez, I. Pavlovic, Zn-Al layered double hydroxides as efficient photocatalysts for NOx abatement, Chem. Eng. J. 346 (2018) 151–158, https://doi.org/10.1016/j.cej.2018.04.022.
[20] X. Lv, J. Zhang, X. Dong, J. Pan, W. Zhang, W. Wang, G. Jiang, F. Dong, layered double hydroxide nanosheets as efficient photocatalysts for NO removal: band structure engineering and surface hydroxyl ions activation, Applied Catalysis B (2020), https://doi.org/10.1016/j.apcatb.2020.119200.
[21] J. Fragoso, J. Balbuena, M. Cruz-Yusta, I. Pavlovic, M. Sánchez, L. Sánchez, Implementing the use of layered double hydroxides as photocatalytic additive for DeNOx building mortars: ZnCr-CO3 a case of study, Constr. Build. Mater. 394 (2023), https://doi.org/10.1016/j.conbuildmat.2023.132241.
[22] H. Li, H. Zhu, Y. Shi, H. Shang, L. Zhang, J. Wang, Vacancy-rich and porous nife-layered double hydroxide ultrathin nanosheets for efficient photocatalytic NO oxidation and storage, Environ. Sci. Technol. 56 (2022) 1771–1779, https://doi.org/10.1021/acs.est.1c07811.
[23] F. Rodriguez-Rivas, A. Pastor, G. de Miguel, M. Cruz-Yusta, I. Pavlovic, L. Sánchez, Cr3+ substituted Zn-Al layered double hydroxides as UV–Vis light photocatalysts for NO gas removal from the urban environment, Sci. Total Environ. 706 (2020) 136009, https://doi.org/10.1016/j.scitotenv.2019.136009.
[24] A. Pastor, F. Rodriguez-Rivas, G. de Miguel, M. Cruz-Yusta, F. Martin, I. Pavlovic, L. Sánchez, Effects of Fe3+ substitution on Zn-Al layered double hydroxides for enhanced NO photochemical abatement, Chem. Eng. J. 387 (2020) 124110, https://doi.org/10.1016/j.cej.2020.124110.
[25] A. Nehdi, N. Frini-Srasra, G. de Miguel, I. Pavlovic, L. Sánchez, J. Fragoso, Use of LDH- chromate adsorption co-product as an air purification photocatalyst, Chemosphere. 286 (2022), https://doi.org/10.1016/j.chemosphere.2021.131812.
[26] J. Fragoso, M.A. Oliva, L. Camacho, M. Cruz-Yusta, G. De Miguel, F. Martin, A. Pastor, I. Pavlovic, L.S. Anchez, Insight into the role of copper in the promoted photocatalytic removal of NO using Zn 2-x Cu x Cr-CO 3 layered double hydroxide, (2021). https://doi.org/10.1016/j.chemosphere.2021.130030.
[27] A. Pastor, C. Chen, G. de Miguel, F. Martín, M. Cruz-Yusta, D. O'Hare, I. Pavlovic, L. Sánchez, Facile synthesis of visible-responsive photocatalytic Eu-doped layered double hydroxide for selective removal of NOx pollutant, Chem. Eng. J. 471 (2023) 144464, https://doi.org/10.1016/j.cej.2023.144464.
[28] S.-F. Ng, M. Yu, L. Lau, W.-J. Ong, engineering layered double hydroxide-based photocatalysts toward artificial photosynthesis: state-of-the-art progress and prospects, Solar Rrl (2020), https://doi.org/10.1002/solr.202000535.
[29] A. Pastor, C. Chen, G. de Miguel, F. Martin, M. Cruz-Yusta, J.C. Buffet, D. O'Hare, I. Pavlovic, L. Sánchez, Aqueous miscible organic solvent treated NiTi layered double hydroxide De-NOx photocatalysts, Chem. Eng. J. 429 (2022), https://doi.org/10.1016/j.cej.2021.132361.
[30] R. Yang, Y. Fan, R. Ye, Y. Tang, X. Cao, Z. Yin, Z. Zeng, MnO2-based materials for environmental applications, Adv. Mater. 33 (2021) 1–53, https://doi.org/10.1002/adma.202004862.
[31] H. Yasmeen, A. Zada, S. Liu, Dye loaded MnO2 and chlorine intercalated g-C3N4 coupling impart enhanced visible light photoactivities for pollutants degradation, J. Photochem. Photobiol. A Chem. 380 (2019) 111867, https://doi.org/10.1016/j.jphotochem.2019.111867.
[32] M.Z.A. Warshagha, M. Muneer, Direct Z-Scheme AgBr/β-MnO2photocatalysts for highly efficient photocatalytic and anticancer activity, ACS Omega. 7 (2022) 30171–30183, https://doi.org/10.1021/acsomega.2c03260.
[33] S. Zhang, L. Zhang, L. Liu, X. Wang, J. Pan, X. Pan, H. Yu, S. Song, NiCo-LDH@MnO2 nanocages as advanced catalysts for efficient formaldehyde elimination, Colloids Surfaces A Physicochem. Eng. Asp. 650 (2022) 129619, https://doi.org/10.1016/j.colsurfa.2022.129619.
[34] J. Wang, H. Zhou, Z. Wang, W. Bai, Y. Cao, Y. Wei, Constructing hierarchical structure based on LDH anchored boron-doped g-C3N4 assembled with MnO2 nanosheets towards reducing toxicants generation and fire hazard of epoxy resin, Compos. Part B Eng. 229 (2022) 109453, https://doi.org/10.1016/j.compositesb.2021.109453.
[35] Z. Ma, L. Fan, F. Jing, J. Zhao, Z. Liu, Q. Li, J. Li, Y. Fan, H. Dong, X. Qin, G. Shao, MnO2Nanowires@NiCo-LDH nanosheet core-shell heterostructure: a slow irreversible transition of hydrotalcite phase for high-performance pseudocapacitance electrode, ACS Appl. Energy Mater. 4 (2021) 3983–3992, https://doi.org/10.1021/acsaem.1c00314.
[36] Q. Wang, D. O'hare, Large-scale synthesis of highly dispersed layered double hydroxide powders containing delaminated single layer nanosheets, Chem. Commun. 49 (2013) 6301–6303, https://doi.org/10.1039/c3cc42918k.
[37] C. Chen, M. Yang, Q. Wang, J.C. Buffet, D. O'Hare, Synthesis and characterisation of aqueous miscible organic-layered double hydroxides, J. Mater. Chem. a. 2 (2014) 15102–15110, https://doi.org/10.1039/c4ta02277g.
[38] M.L. López, I. Álvarez-Serrano, D.A. Giraldo, P. Almodóvar, E. Rodríguez-Aguado, E. Rodríguez-Castellón, Influence of MnO2-birnessite microstructure on the electrochemical performance of aqueous zinc ion batteries, Appl. Sci. 12 (2022), https://doi.org/10.3390/app12031176.
[39] V.A. Drits, B. Lanson, A.C. Gaillot, Birnessite polytype systematics and identification by powder X-ray diffraction, Am. Mineral. 92 (2007) 771–788, https://doi.org/10.2138/am.2007.2207.
[40] H. Yin, Z. Tang, Ultrathin two-dimensional layered metal hydroxides: An emerging platform for advanced catalysis, energy conversion and storage, Chem. Soc. Rev. 45 (2016) 4873–4891, https://doi.org/10.1039/c6cs00343e.
[41] F.T. Ling, J.E. Post, P.J. Heaney, J.D. Kubicki, C.M. Santelli, Fourier-transform infrared spectroscopy (FTIR) analysis of triclinic and hexagonal birnessites, Spectrochim. Acta - Part A Mol. Biomol. Spectrosc. 178 (2017) 32–46, https://doi.org/10.1016/j.saa.2017.01.032.

[42] J. Zhao, J. Nan, Z. Zhao, N. Li, J. Liu, F. Cui, Energy-efficient fabrication of a novel multivalence Mn3O4-MnO2 heterojunction for dye degradation under visible light irradiation, Appl. Catal. B Environ. 202 (2017) 509–517, https://doi.org/10.1016/j.apcatb.2016.09.065.
[43] M. Dung Nguyen, T. Binh Nguyen, L. Hai Tran, T. Giang Nguyen, I. Fatimah, E. Prasetyo Kuncoro, R.A. Doong, S. Z-scheme, B co-doped g-C3N4 nanotube@MnO2 heterojunction with visible-light-responsive for enhanced photodegradation of diclofenac by peroxymonosulfate activation, Chem. Eng. J. 452 (2023) 139249, https://doi.org/10.1016/j.cej.2022.139249.
[44] A.S. Belousov, E.V. Suleimanov, A.A. Parkhacheva, D.G. Fukina, A.V. Koryagin, A. V. Koroleva, E.V. Zhizhin, A.P. Gorshkov, Regulating of MnO2 photocatalytic activity in degradation of organic dyes by polymorphic engineering, Solid State Sci. 132 (2022) 106997, https://doi.org/10.1016/j.solidstatesciences.2022.106997.
[45] J. Richard, Lewis, Sax's dangerous properties of industrial materials, 12th ed., Hoboken, New Jersey, 2012.
[46] Y. Jing, A. Fan, J. Guo, T. Shen, S. Yuan, Y. Chu, Synthesis of an ultrathin MnO2 nanosheet-coated Bi2WO6 nanosheet as a heterojunction photocatalyst with enhanced photocatalytic activity, Chem. Eng. J. 429 (2022) 132193, https://doi.org/10.1016/j.cej.2021.132193.
[47] F. Shabib, R. Fazaeli, H. Aliyan, D. Richeson, Hierarchical mesoporous plasmonic Pd-Fe3O4/NiFe-LDH composites: characterization, and kinetic study of a photodegradation catalyst for aqueous metoclopramide, Environ. Technol. Innov. 27 (2022) 102515, https://doi.org/10.1016/j.eti.2022.102515.
[48] Y. Zhang, M. Wu, Y.H. Kwok, Y. Wang, W. Zhao, X. Zhao, H. Huang, D.Y.C. Leung, In-situ synthesis of heterojunction TiO2/MnO2 nanostructure with excellent performance in vacuum ultraviolet photocatalytic oxidation of toluene, Appl. Catal. B Environ. 259 (2019) 118034, https://doi.org/10.1016/j.apcatb.2019.118034.
[49] Y. Li, X. Wang, H. Huo, Z. Li, J. Shi, A novel binary visible-light-driven photocatalyst type-I CdIn2S4/g-C3N4 heterojunctions coupling with H2O2: synthesis, characterization, photocatalytic activity for Reactive Blue 19 degradation and mechanism analysis, Colloids Surfaces A Physicochem. Eng. Asp. 587 (2020) 124322, https://doi.org/10.1016/j.colsurfa.2019.124322.
[50] J.F.M. and G.E.M.P.C. C. D. Wanger, W. M. Riggs, L. E. Davis, Handbook of X-ray Photoelectron Spectroscopy, Minnesota, USA, 1992.
[51] K. Lei, X. Han, Y. Hu, X. Liu, L. Cong, F. Cheng, J. Chen, Chemical etching of manganese oxides for electrocatalytic oxygen reduction reaction, Chem. Commun. 51 (2015) 11599–11602, https://doi.org/10.1039/c5cc03155a.
[52] M. Toupin, T. Brousse, D. Bélanger, Charge storage mechanism of MnO2 electrode used in aqueous electrochemical capacitor, Chem. Mater. 16 (2004) 3184–3190, https://doi.org/10.1021/cm049649j.
[53] K.D. Elke Beyreuther, S. Grafström, L.M. Eng, Christian Thiele, XPS investigation of Mn valence in lanthanum manganite thin films under variation of oxygen content, Phys. Rev. b. 73 (2006) 155425, 101103/PhysRevB.3.155425.
[54] M. Fujiwara, T. Matsushita, S. Ikeda, Evaluation of Mn3s X-ray photoelectron spectroscopy for characterization of manganese complexes, J. Electron Spectros. Relat. Phenomena. 74 (1995) 201–206, https://doi.org/10.1016/0368-2048(94)02375-1.
[55] G.M.R. and E.J. RAUCKMAN, Spin Trapping of the Primary Radical Involved in the Activation of the Carcinogen N-Hydroxy-2-acetylaminofluorene by Cumene Hydroperoxide-Hematin, Mol. Pharmacol. 17 (1980) 233–238. https://doi.org/0026-895X/80/020233-06$02.00/0.
[56] E. Finkelstein, G.M. Rosen, E.J. Rauckman, Spin trapping of superoxide and hydroxyl radical: Practical aspects, Arch. Biochem. Biophys. 200 (1980) 1–16, https://doi.org/10.1016/0003-9861(80)90323-9.
[57] J. Liu, F. An, M. Li, L. Yang, J. Wan, S. Zhang, Efficient Degradation of 2,4-Dichlorophenol on Activation of Peroxymonosulfate Mediated by MnO2, Bull. Environ. Contam. Toxicol. 107 (2021) 255–262, https://doi.org/10.1007/s00128-021-03109-7.
[58] D.D.G. Qiyu Lian, Lingling Hu, Dingren Ma, Yimu Jiao, Dehua Xia, Yajing Huang, Zhuoyun Tang, Wei Qu, Huinan Zhao, Chun He, Interstitial Atomic Bi Charge-Alternating Processor Boosts Twofold Molecular Oxygen Activation Enabling Rapid Catalytic Oxidation Reactions at Room Temperature, Adv. Funct. Mater. 32 (2022) 2205054. https://doi.org/10.1002/adfm.202205054.
[59] W. Huo, W. Xu, T. Cao, Z. Guo, X. Liu, G. Ge, N. Li, T. Lan, H.C. Yao, Y. Zhang, F. Dong, Carbonate doped Bi2MoO6 hierarchical nanostructure with enhanced transformation of active radicals for efficient photocatalytic removal of NO, J. Colloid Interface Sci. 557 (2019) 816–824, https://doi.org/10.1016/j.jcis.2019.09.089.
[60] X. Li, W. Zhang, W. Cui, J. Li, Y. Sun, G. Jiang, H. Huang, Y. Zhang, F. Dong, Reactant activation and photocatalysis mechanisms on Bi-metal@Bi2GeO5 with oxygen vacancies: a combined experimental and theoretical investigation, Chem. Eng. J. 370 (2019) 1366–1375, https://doi.org/10.1016/j.cej.2019.04.003.
[61] P. Chen, H. Liu, Y. Sun, J. Li, W. Cui, L. Wang, W. Zhang, X. Yuan, Z. Wang, Y. Zhang, F. Dong, Bi metal prevents the deactivation of oxygen vacancies in Bi2O2CO3 for stable and efficient photocatalytic NO abatement, Appl. Catal. B Environ. 264 (2020) 118545, https://doi.org/10.1016/j.apcatb.2019.118545.
[62] W. Huo, W. Xu, T. Cao, X. Liu, Y. Zhang, F. Dong, Carbonate-intercalated defective bismuth tungstate for efficiently photocatalytic NO removal and promotion mechanism study, Appl. Catal. B Environ. 254 (2019) 206–213, https://doi.org/10.1016/j.apcatb.2019.04.099.
[63] W. Huo, T. Cao, W. Xu, Z. Guo, X. Liu, H.C. Yao, Y. Zhang, F. Dong, Facile construction of Bi2Mo3O12@Bi2O2CO3 heterojunctions for enhanced photocatalytic efficiency toward NO removal and study of the conversion process, Chinese, J. Catal. 41 (2020) 268–275, https://doi.org/10.1016/S1872-2067(19)63460-1.
[64] W. Zhang, X. Dong, Y. Liang, Y. Sun, F. Dong, Ag/AgCl nanoparticles assembled on BiOCl/Bi 12 O 17 Cl 2 nanosheets: enhanced plasmonic visible light photocatalysis and in situ DRIFTS investigation, Appl. Surf. Sci. 455 (2018) 236–243, https://doi.org/10.1016/j.apsusc.2018.05.171.
[65] F.F. Marafatto, M.L. Strader, J. Gonzalez-Holguera, A. Schwartzberg, B. Gilbert, J. Peña, Rate and mechanism of the photoreduction of birnessite (MnO2) nanosheets, Proc. Natl. Acad. Sci. u. s. a. 112 (2015) 4600–4605, https://doi.org/10.1073/pnas.1421018112.